Advances in Science and Technology Research Journal

Advances in Science and Technology Research Journal, 2025, 19(10), 329–346
https://doi.org/10.12913/22998624/208173
ISSN 2299-8624, License CC-BY 4.0

Received: 2025.06.12
Accepted: 2025.08.15
Published: 2025.09.01

Mobile ultrasound-impedance tomograph for long-term monitoring of the lower urinary tract: Optimization of miniaturization and electromagnetic compatibilit

Tomasz Rymarczyk[1,2*], Michał Gołąbek[1], Grzegorz Kłosowski[3], Józef Stokłosa[2], Mariusz Kalita[2], Edward Kozłowski[3]

[1] Research & Development Centre Netrix S.A., ul. Związkowa 26, 20-704 Lublin, Poland
[2] WSEI University, ul. Projektowa 4, 20-209 Lublin, Poland
[3] Lublin University of Technology, ul. Nadbystrzycka 38D, 20-618 Lublin, Poland
* Corresponding author's e-mail: tomasz@rymarczyk.com

ABSTRACT

The paper presents the design, development, and optimization of a hybrid mobile tomograph integrating ultrasound tomography (UST) and electrical impedance tomography (EIT) for long-term, non-invasive monitoring of the lower urinary tract. The proposed solution is characterized by the integration of miniaturized and energy-efficient electronic modules within a wearable system, facilitating wireless communication and real-time data acquisition. The final prototype incorporates advanced power management, customized sensor systems, and the integration of UST beamforming and EIT signal acquisition. Comprehensive electromagnetic compatibility (EMC) and electrostatic discharge (ESD) tests were conducted in compliance with medical device standards (PN-EN 60601-1-2), thereby confirming the tomograph's suitability for clinical and home healthcare environments. The findings indicate that the hybrid approach enhances diagnostic imaging while ensuring safety, comfort, and mobility for patients, particularly in pediatric applications. The solution contributes to the advancement of smart medical diagnostic tools in biomedical engineering.

Keywords: ultrasound tomography, electrical tomography, energy optimization, electromagnetic compatibility.

INTRODUCTION

Children often suffer from urinary tract disorders. Approximately 7–10% of children over the age of 5 suffer from urinary incontinence. Genetic, demographic, environmental, behavioral, or physical factors may be the cause of this dis/order [1]. Serious consequences, including kidney damage and urosepsis, can result from neglected disorders [2]. Because of the complexity of the problem, accurate diagnosis is essential for successful therapy. Due to the prevalence of bladder abnormalities and disorders, especially in the pediatric population, innovative methods for accurate diagnosis and treatment are needed. As a result, researchers are trying to develop new ways to diagnose and treat these conditions.

In recent years, there have been significant advances in imaging techniques such as ultrasound and magnetic resonance imaging (MRI) for assessing the urinary tract. New pharmacological and non-invasive treatments have been developed [3, 4]. However, more research is needed to fully understand the causes of these disorders and determine the most effective methods of diagnosis and treatment. In response to these problems, a hybrid CT scanner was developed with the unique ability to provide real-time, non-invasive imaging that goes beyond the limits of conventional methods. It combines two imaging techniques – ultrasound tomography (UST), and ielectrical impedance tomography (EIT). The UST system uses advanced beam modeling technology to concentrate and control the ultrasound wave to generate images of the

body's tissue structures. Measurements are made using a phased array ultrasonic probe. The EIT system images the body's electrical conductivity using low-frequency electric currents. The device uses a set of dedicated electrodes to measure impedance. The insert with electrodes is an integral part of the measurement system. Combining these two technologies allows for optimizing the underlying physical and chemical processes. The synergistic combination of diverse technologies often leads to enhanced capabilities, providing researchers and practitioners with a more comprehensive understanding of complex systems [5].

Artificial intelligence is employed to address various challenges in science and industry [6–10]. Innovative algorithms adapted to a hybrid imaging system are intended to increase diagnostic capabilities in medical diagnostics. This hybrid system integrates UST and EIT. The algorithms employed aim to interpret complex data generated simultaneously by UST and EIT, facilitating early detection of irregularities and providing appropriate information. Consequently, this synergistic approach enhances the potential for early detection of bladder diseases.

The key challenge was to develop miniaturized functional modules of the system, which were aimed at two important benefits: increasing the device's portability and optimizing its energy efficiency. This process required precise optimization of each component to achieve a more compact form while maintaining full functionality. Thanks to the above tasks, the device has become entirely mobile, which means it can be easily carried by the patient and used in different places while maintaining full functionality. Miniaturized modules also positively impacted the aesthetics and ergonomics of the device. Optimizing energy efficiency was also an extremely important aspect of the solution design process. Thanks to optimized modules and more efficient energy solutions, the device can operate longer on a single charge, increasing its usability and usefulness for users. As a result, an energy-balanced device is an important step towards modern and efficient technologies. Similar challenges related to embedded system design and energy optimization have also been discussed in other engineering domains, including precision agriculture applications [11].

This study addresses current challenges in urinary tract diagnostics by introducing a hybrid imaging system that integrates UST and EIT in a portable, long-term monitoring device. While previous studies have explored these modalities separately or in stationary settings, the proposed system represents a novel scientific contribution by integrating both techniques into a single, portable platform designed for continuous, real-time diagnostics outside of clinical facilities.

The originality of this work lies in the fusion of complementary physical modalities – ultrasound propagation and tissue conductivity - into a miniaturized system that allows simultaneous structural and functional assessment in mobile conditions. This integration is supported by a novel methodological approach to signal synchronization and reconstruction that ensures stable and accurate multimodal imaging. In addition, the system introduces an innovative energy-efficient hardware architecture capable of high-speed operation and meeting stringent electromagnetic compatibility (EMC) standards for medical devices, an aspect rarely addressed in similar designs. As such, the solution presented advances the field of multimodal biomedical engineering and can serve as a reference model for future intelligent diagnostic platforms targeting pediatric and ambulatory care.

MATERIALS AND METHODS

Medical ultrasonic tomography is usually associated with large ultrasound devices and a complex medical examination combined with the participation of a doctor. Ultrasound imaging as a stand-alone test has certain constraints or limitations [12]. Such examinations are not a problem for adults, but younger patients can be uncomfortable, especially if they are to be monitored for an extended period, similar to a Holter examination.

The main goal of the project and the challenge was to design a tomographic device that is mobile, wearable, wireless, and can monitor the urinary system in real-time using UST [13] and EIT [14]. Due to its complexity, the project went through a long and complicated prototyping process.

The hybrid computed tomography scanner, designed for noninvasive real-time imaging of urinary tract diseases, combines two technologies, including the meticulous selection of electronic components and an advanced algorithm. A focus on energy efficiency and optimization was integral to the device design process. The device's hardware consists of several components, each playing a key role in achieving its innovative capabilities.

The prototyping process

The initial prototype construction allowed for testing key components of the ultrasonic measurement system (Figure 1). It supported 16 ultrasonic channels. The test setup was created using an STM32H7 microcontroller connected via a parallel FMC bus to an Intel Cyclone IV FPGA and two MAX2082 devices [15]. These devices are integrated 8-channel circuits containing elements necessary for generating ultrasonic excitation and acquiring ultrasonic signals from a phased array of ultrasonic transducers. Additionally, high-voltage power converters (+/-72V) were placed on the board to supply power to the ultrasonic excitation circuits. Ultimately, the test setup exposed several issues addressed in the subsequent version.

The subsequent construction was expanded to a 32-channel ultrasonic tomography system and divided into measurement cards. Connecting a single FPGA with a single MAX2082 instead of two allowed for synthesizing properly functioning software and provided adequate SRAM memory for captured measurement data. This configuration also reduced crosstalk levels between LVDS differential transmission and single-ended FMC transmission.

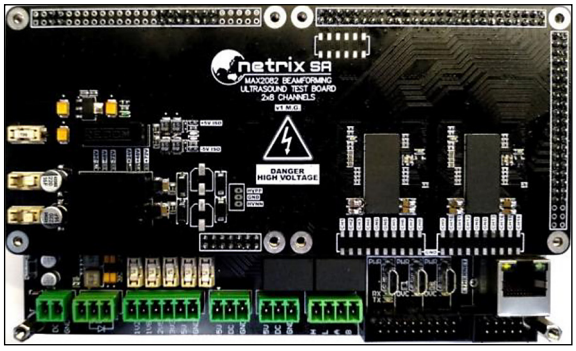

Figure 1. The first prototype of a 16-channel ultrasonic tomograph was developed to test the key components of the system

The modular construction simplified assembly and ensured better heat dissipation. Due to the initial assumption that the tomograph would be hybrid, combining both ultrasonic and impedance tomography, another solution was designed (Figure 2).

In the following version, the tomograph was expanded to 64 ultrasonic channels using 2:1 multiplexers and was designed for use with medical ultrasonic probes for abdominal cavity examination. As mentioned earlier, the tomograph has been enhanced to include the capability for impedance tomography measurements. An additional measurement card supporting 16 channels for measuring the impedance of the human body with a current excitation up to 100 µA at 100 kHz has been integrated (Figure 3). The design enabled experiments using a 128-channel ultrasound transducer head, specifically the Philips C5-2 model (Figure 4). The integration of signal multiplexers within the transducer head allowed for the handling of such a large number of ultrasound channels [16–18].

Several housing variants were designed for the new solution, and ultimately, the version with a white housing, gold logo, and a colored LED strip to indicate the device's operational status was chosen. The housing was produced using stereolithography (SLA) 3D printing. Enclosing the electronics in the housing improved its safety against accidental damage and allowed for experiments on phantoms (Figure 5).

The first fully functional and stable construction of the tomograph for monitoring the lower urinary tract, equipped with ultrasonic and impedance tomography, was a stationary version, not optimized for energy efficiency, and lacked wireless communication. Due to this, the decision was made to adopt another improvement to the existing design as the primary solution. At this stage, an analysis was also performed on the

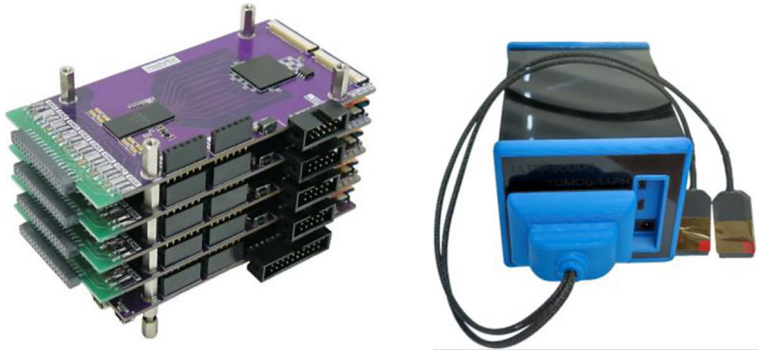

Figure 2. The second prototype of the 32-channel ultrasonic tomograph, divided into measurement cards

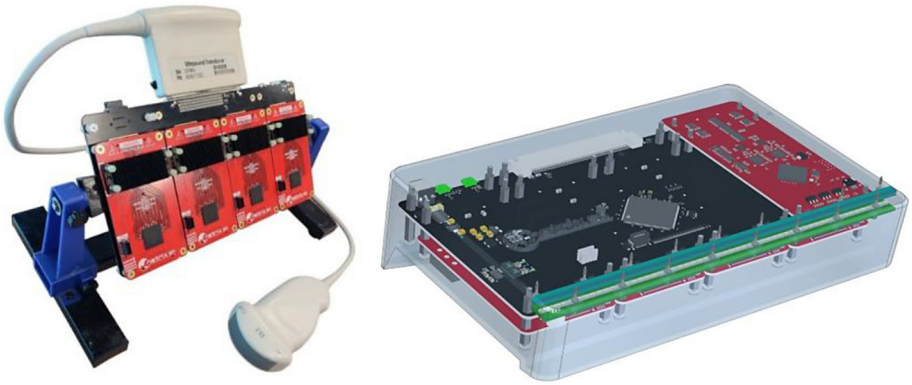

Figure 3. The third version of the prototype tomograph designed for monitoring the lower urinary tract, featuring an integrated 64-channel ultrasound tomography and a 16-channel electrical impedance tomography

Figure 4. Internal construction of the 128-channel Philips C5-2 transducer head

Figure 5. The third version of the tomograph is used to study the lower urinary tract during measurements on phantoms, along with the measured signal from a single channel of the ultra-sound transducer head

arrangement of all electronic components relative to each other, ensuring that the designed device could be mobile, highly miniaturized, and ergonomic. The subsequent version of the tomograph was improved in these aspects and represents the final design of the device.

Final hardware design ensuring mobility and energy efficiency

The final version of the tomograph has been completely redesigned in terms of appearance, usability, and power supply. The new version is fully portable and designed as a compact backpack. The housing dimensions are minimal (tailored to electronic components). Simultaneously, the part adjacent to the back remains flat. Comfort during wear will be enhanced by foam attached to the rear part of the housing and a spacer mesh attached to the backpack straps. Power cells are positioned to ensure an even distribution of the device's weight. At the same time, the design allows for the detachment of the module and removal of the cells for replacement. Specially designed handles are incorporated into the housing to fasten with the straps securely. The miniaturization of

the device results in a high power density of the device [19], which is why it was so important to take care of heat dissipation. Ventilation openings are integrated into the design to facilitate the dissipation of warm air from the housing. An LED strip complements the aesthetics and serves as a communication link between the device and the user. The housing body is made of PA-12 using SLS printing technology (Figure 6).

Each circuit in the new design has the capability of remote power control. Critical circuits, such as the STM32H7 microcontroller and the ESP32 Wi-Fi communication board, are powered by a highly efficient LMR12020 converter operating at a frequency of 2MHz throughout the entire device's operation. On the other hand, the power supply to the UST and EIT measurement cards can be disconnected during breaks between consecutive measurements, allowing for significantly lower energy consumption stored in the batteries (Figure 7a).

The new design has also changed the method of generating high voltage. The new model of HV converters necessary for developing the excitation signal of the phased measurement head operates in SEPIC technology [20]. This allows these converters to work with much greater efficiency and voltage stability than the previously used compact NMT1272SC converters with galvanic isolation. Depending on the load, the new LT3958 converters also have much better and more stable temperature characteristics (Figure 7b).

The new main board design includes an integrated BMS (battery management system) for four 18650 battery cells, which is necessary for optimizing the energy efficiency of the charging process. The main board is also equipped with a Li-Ion battery charger using the LTC4006EGN-4

Figure 6. 3D model of UST & EIT tomograph construction

circuit. An important aspect of the device design was developing a sensor system that enables simultaneous measurements using ultrasonic tomography and impedance. One of the challenges to overcome was developing a method

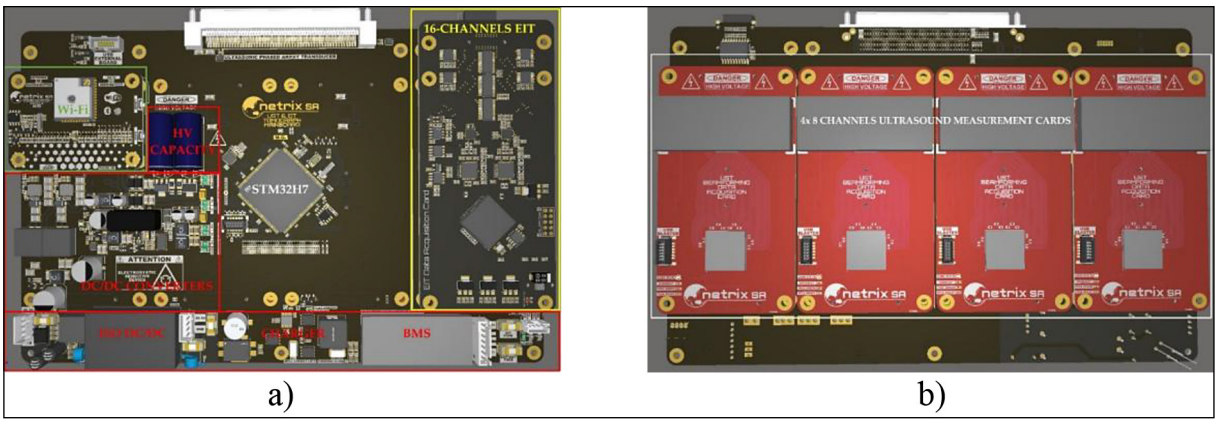

Figure 7. The final version of the main board for the tomograph monitoring the lower urinary tract: (a) top view, (b) bottom view

for mounting sensors on the patient's body at the bladder level (Figure 8).

The STM32H7 microcontroller serves as the basis for the main board. It enables communication with the impedance measurement card via UART and QUAD SPI, and provides parallel FMC data transfer from ultrasonic measurement cards at a rate of 100 MHz. The motherboard also includes a Wi-Fi module and USB 1.0 and USB 2.0 communication interfaces for connection to the image reconstruction system. In addition, the motherboard provides each module with the appropriate power levels.

The board is made of six-layer copper and manufactured on a 2 mm thickness PCB to ensure the best separation of high-voltage signals from connected ultrasound measurement cards. Each UST measurement card has eight measurement channels, resulting in 32. The motherboard also has built-in 2:1 multiplexers, which allows multiplying UST channels up to 64. The UST cards are synchronized by a standard clock, allowing control of the excitation on each channel with an accuracy of up to 1ns. This feature is required for ultrasound beamforming measurements [21–24] (Figure 9).

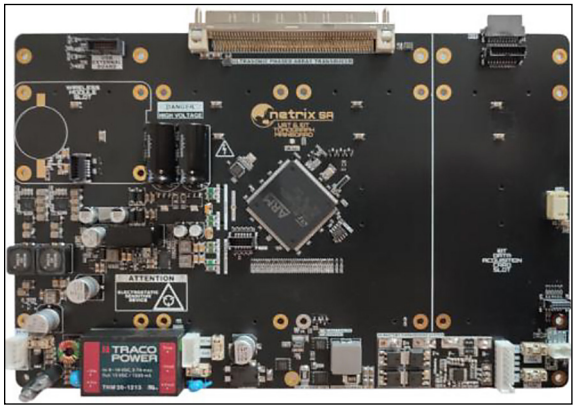

Figure 8. The final version of the tomograph mainboard for monitoring the lower urinary tract

Beamforming technology gives the ability to perform a large number of reflection measurements using a small number of channels/transducers (and their number is mainly due to the step with which the phase of the transmitting signal will be shifted). The phase shift on each of the transmitting transducers allows for the direction of the wave beam at a specific angle, thanks to which, using static transducers, it is possible to image similarly to using one transducer with a mechanically controlled angle/direction. Beamforming also allows the ultrasonic wave to be focused at a point, making it possible to inspect the object sector by sector.

The UST measurement card includes an octal-channel measurement integrated circuit MAX2082 from Maxim and an FPGA Altera Cyclone IV from Intel. The MAX2082 contains 8x high-voltage 3-level 2A Pulses, 8x T/R switchers, 8x low-noise amplifiers (LNA), 8x variable-gain amplifiers (VGA), 8x anti-aliasing filters (AAF), 8x ADC 12 bit 50 MSPS, and 8x Digital High-Pass Filters (Figure 10).

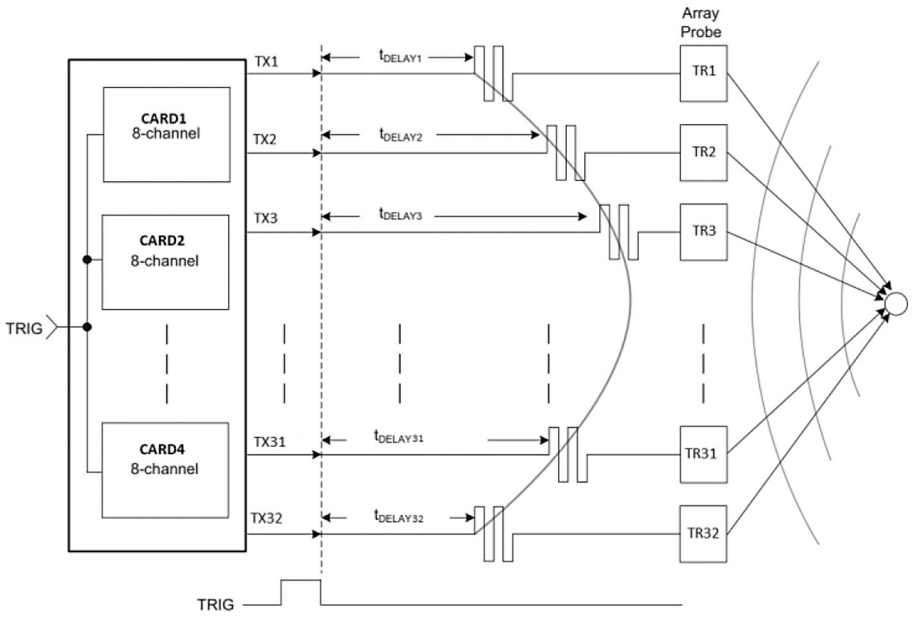

Figure 9. Ultrasonic beamforming implementation

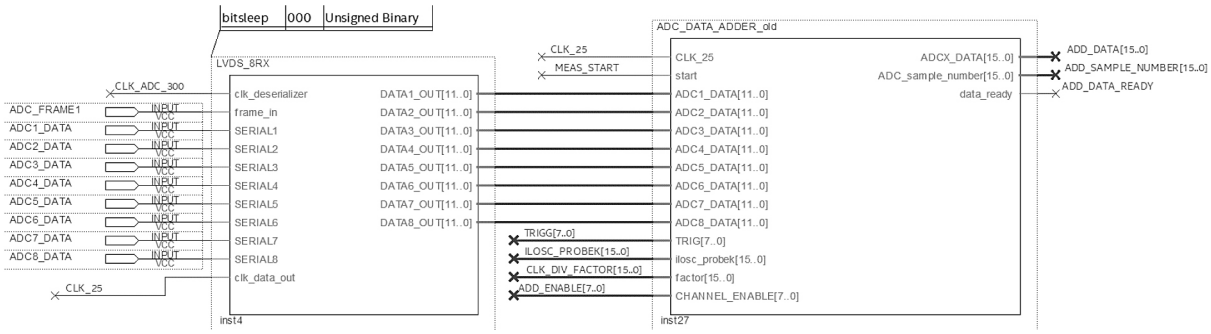

Figure 10. Implementation of measurement data deserialization and summation in phase

The above figure shows the data acquisition method from a single MAX2082 chip. The phase-shifted measurement data are deserialized in the first block with the 300MHz clock from the MAX2082 chip. Using a 25 MHz clock, data from 8 ADCs are fed simultaneously to the summation block. Based on the table of delays for eight channels, this block receives eight trigger signals (TRIG[7..]), which sums up data from all channels with a given delay. The summed output data (ADCX_DATA[15..0]) are transferred to the FPGA's internal RAM, from where, using the FMC bus, they are loaded to the STM32H7 microcontroller along with data from other measurement cards, where the already completed data are added up, as a result of which the result of a single sample measurement is 17 bits. The number of measurements per one measurement matrix is set with the parameter ILOSC_PROBEK [15..0]. This number is 16-bit, but due to the limited amount of RAM available in the FPGA and the STM32H7 microcontroller, this number is limited to 10000 sample measurements (Figure 11).

Before measurements, the mainboard parameterizes the UST cards. They send data about delays on each channel, the number of measurement samples, excitation frequency, pulses, filtering, and active channels. The standard clock and the low state on the GPIO trigger line are responsible for accurately synchronizing the start of measurements. The collected data are summed up based on the delay data to create a common 16-bit measurement vector and are sent via FMC and USB or Wi-Fi to the image reconstruction system (Figure 12).

The EIT measurement card provides impedance measurements using 16 electrodes made of silver and covered with gold. The voltage and current values are measured using the ADC converter system from Linear Technology LTC2203, which has a sampling rate of up to 25 Msps and uses a pipelined architecture with a built-in PGA. Data transmission to the FPGA is performed using a parallel bus. Current excitation is achieved using digital-to-analog converters. The FPGA system controls two DAC8830 converters using a serial bus. The converters work concurrently,

Figure 11. Ultrasound 8-channel beamforming measuring card

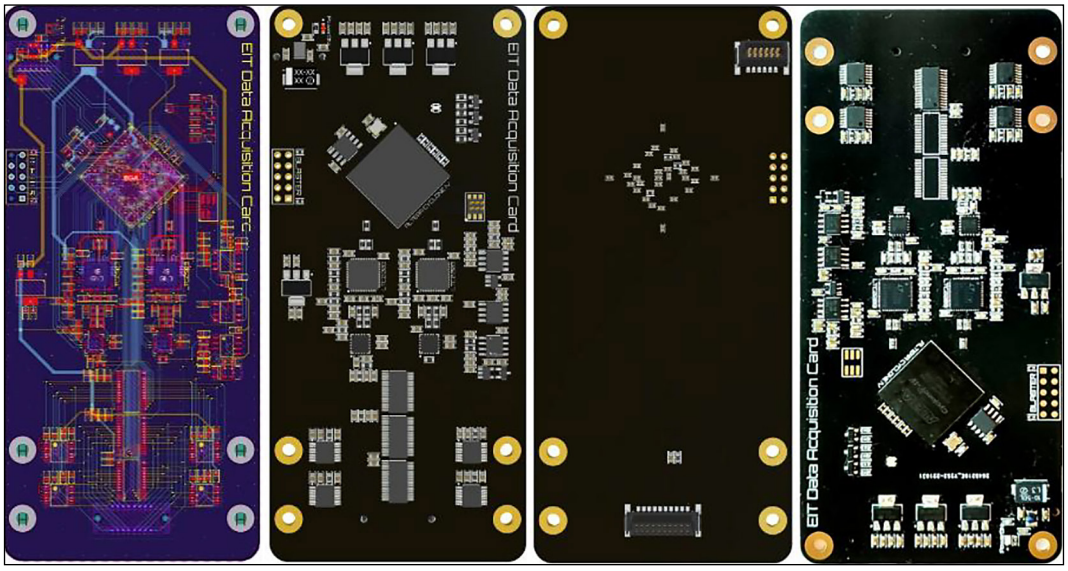

Figure 12. Electrical impedance 16-channel measuring card

with one converter's output being used as a reference signal for the other. This enables the system to generate any waveform shape while maintaining the necessary resolution for digital control of amplitude (Figure 13).

The wireless communication of the hybrid tomograph for monitoring the lower urinary tract was implemented using the ESP32 Wi-Fi module with an external antenna installed inside the housing. The module was programmed to operate as an access point. The device can function in any conditions as it doesn't require connection to external networks; it's sufficient to connect to the network broadcasted by the device. Internal communication between the ESP32 module and the main STM32H7 microcontroller was achieved using the SPI bus (to transmit measurement data) and UART (to control the measurement sequence and parameterization).

Measurement sensors

An essential aspect of the device design was developing a measurement sensor system that enables simultaneous measurement using ultrasonic tomography and impedance. One of the challenges to overcome was developing a method for mounting sensors on the patient's body at the bladder level. Developing the best solution for making electrodes and selecting the appropriate electrically conductive material was important.

The first concept of the electrode system is a belt with attached textile measurement points. A problematic aspect of this variant was the lack of possibility for proper cleaning and disinfection (Figure 14).

The design of the measurement system has been improved. Textile electrodes have been attached to a silicone insert. Dedicated underwear and a pocket for electrodes attached to Velcro have been designed for this solution. However, tests of this solution did not yield satisfactory results. In the next version, textile electrodes were replaced with measurement points in approximately 5 mm diameter spheres made of silver coated with gold. The convex shape of the spheres ensured proper contact pressure. The material they are made of allows for thorough disinfection. An optimal solution was achieved by improving each

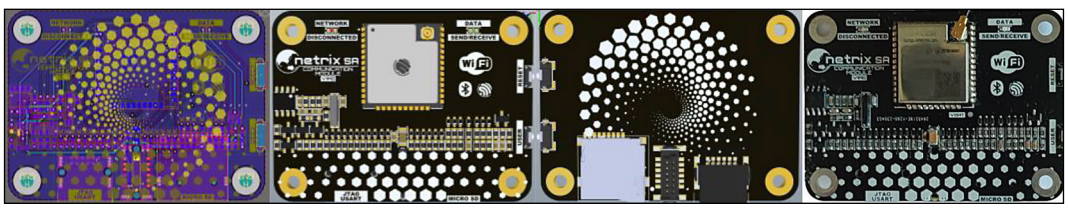

Figure 13. The Wi-Fi wireless communication module

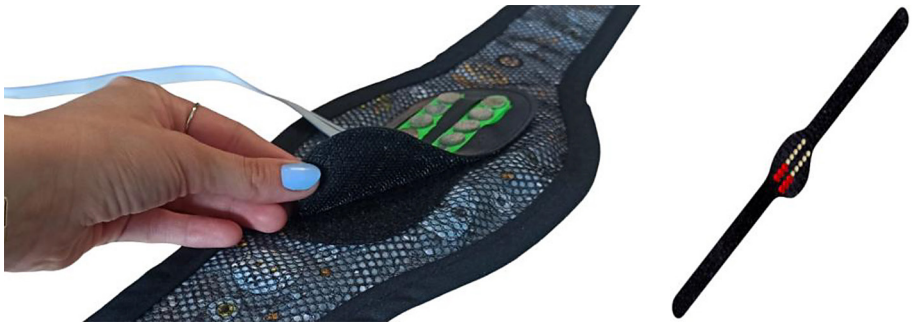

Figure 14. First concept (right) and prototype (left) of the electrode system as belt with attached textile measurement electrodes for impedance measurement

subsequent version of the measurement sensors. The developed solution is a probe with electrodes mounted on dedicated underwear. The probe has an electrode arrangement optimized for EIT and UST measurements. It has been designed to allow easy and secure connection to the measurement system. A crucial aspect was maintaining a balance between wearing comfort and electrode contact quality.

A pocket attached with Velcro to the underwear was chosen to achieve optimal electrode fit and improve signal conduction. The electrode insert can be easily inserted and removed from this pocket. This solution represents a compromise between effective electrode pressure, simplicity of installation, disinfection capability, and patient comfort during examination. With this approach, the insert becomes universal for different body types of patients, and adjusting its size only requires adjusting the textile underwear using Velcro straps (Figure 15). The electrode assembly involves the following steps:

1. Inserting the electrode system into the insert.
2. Fasten the strap located in the insert.
3. Securing the insert with electrodes onto the dedicated garment.
4. Routing the plug through the dedicated opening in the garment.

The EIT measurement electrode system consists of 16 electrically conductive measuring points. The wires leading to the measuring points are carefully protected and concealed inside the insert to isolate them from the patient's body. A mounting hole for the dedicated UST transducer was designed in the middle of the insert. The ultrasonic transducer was designed for the measurement system and adapted for imaging the bladder. Additionally, its physical construction allows adaptation to human anatomical structure, ensuring comfort during measurements. The applied transducer has a linear 32-channel array of transducers with a step of 500 µm, a maximum focusing depth of about 13 cm, and a rotation angle of +/-30° [25].

RESULTS – ELECTROMAGNETIC COMPATIBILITY (EMC)

The Accredited Laboratory of Electromagnetic Compatibility at the Wroclaw University of Science and Technology in Poland conducted tests on the tomograph for monitoring the lower urinary tract. The purpose of the tests was to verify the device's suitability for use in the "environment of professional healthcare facilities and home healthcare" as defined by PN-EN

Figure 15. Textile underwear for hybrid UST/EIT sensor

60601-1-2 [26]. The initial tests were conducted during the device's design phase to identify issues and proactively prepare it for subsequent certification examinations. As part of the research, the following tests were conducted:

EMC immunity testing:
- Electrical fast transient (EFT) immunity tests according to PN-EN 61000-4-4 [27].
- Surge immunity tests according to PN-EN 61000-4-5 [28].
- ESD immunity tests according to PN-EN 61000-4-2 [29].
- Burst transient immunity tests according to PN-EN 61000-4-4 [27].
- Conducted immunity test according to PN-EN 61000-4-6 [30].
- Radiated immunity tests according to PN-EN 61000-4-3 [31].
- Magnetic field immunity test at a frequency of 50Hz according to PN-EN 61000-4-8 [32].
- Voltage Dips, Drops & Interruptions immunity test according to PN-EN 61000-4-11 [33].

Emission tests:
- Conducted emissions tests according to PN-EN 55016-2-1 [34].
- Radiated emissions tests in the frequency range from 30 MHz to 1 GHz, radiated at a distance of 10 meters according to PN-EN 55016-2-3 [35].
- Radiated emissions tests in the frequency range from 1 GHz to 6 GHz, radiated at a distance of 3 meters according to PN-EN 55016-2-3 [35].
- Harmonic tests according to PN-EN 61000-3-2 [36].
- Flicker tests according to PN-EN 61000-3-3 [37].

Due to the extensive number of tests conducted, only a few selected ones are presented and discussed below.

Conducted emissions tests

Conducted disturbances measurements have been carried out according to the procedure defined in PN-EN 55011 [38], PN-EN 55032 [39] and PN-EN 55016-2-1 [34] standards as required in PN-EN 60601-1-2 [26] (Figure 16). Asymmetrical high-frequency conducted disturbances inducted by the equipment under test (EUT) at the power supply port are measured using an Artificial Mains Network and the EMI receiver in the frequency range from 150 kHz to 30 MHz for each of the two lines (L and N). The measurements for the EUT were performed in the shielded room (Figure 16) [40]. The UST/EIT tomograph equipment under test was connected to the Artificial Mains Network and located 40 cm above the reference ground plane (shielded room's floor) on charging mode, using the Mean Well GSM60B18-P1J charger. An excess of the mains cable was bundled to provide a distance of 80 cm between the EUT and the AMN.

Preliminary measurements of conducted emissions for the UST/EIT tomograph confirmed compliance with class B, group 1 limits specified in PN-EN 55011 [38] and PN-EN 55032 [39] standards. The results demonstrated that the highest measured values across the 150 kHz to 30 MHz frequency range remained within the permissible limits for both quasi-peak and average detectors. Minor peaks close to the threshold were observed and addressed through design refinements in subsequent versions of the device.

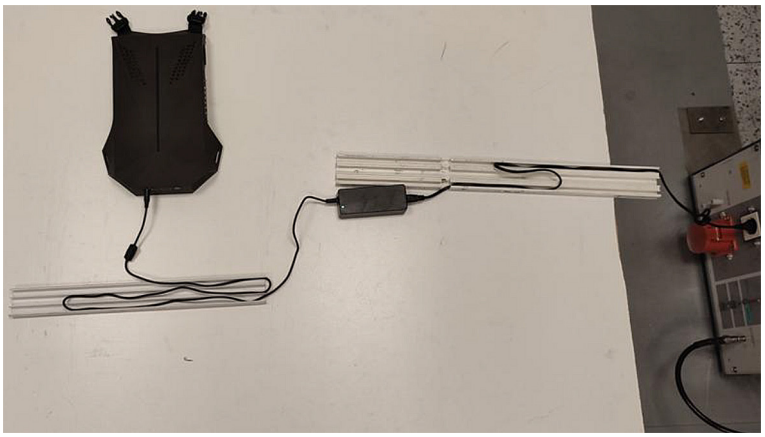

Figure 16. UST/EIT tomograph for monitoring the lower urinary conducted emissions tests

Radiated emissions tests in the frequency range from 30 MHz to 1 GHz, radiated at a distance of 10 meters

Electromagnetic compatibility testing was conducted in the frequency range from 30 MHz to 1 GHz and from 1 GHz to 6 GHz. Measurements have been carried out according to the procedure defined in PN-EN 55016-2-3 [35], PN-EN 55011 [38] and PN-EN 55032 standards as required in PN-EN 60601-1-2 [26].The tests allowed for identifying electromagnetic field sources exceeding permissible standards. The detected issues mainly stemmed from insufficient filtering of internal signals that passed through the wiring outside the device. During the first tests (design tests), identified problems were systematically addressed, and measurements were repeated until emission source elimination surpassed the final certification test standards.

In the 30 MHz to 1 GHz frequency range, the tomograph was positioned on a mannequin simulating realistic clinical use, while the measurement antenna was mounted on an automatically adjustable mast (height range: 1 to 4 meters, with vertical and horizontal polarization changes). The test setup included a rotating table enabling 360° rotation in 45° increments. Initial measurements showed that instantaneous emission levels exceeded the regulatory limits in several frequency bands, particularly between 30 MHz and 100 MHz. These anomalies were attributed to the 100 MHz internal clock and long parallel bus lines of the UST cards. Appropriate filtering and layout modifications were implemented, which ultimately reduced emissions to compliant levels. Final quasi-peak measurements confirmed full conformity with class B, group 1 device limits specified in PN-EN 55011 and PN-EN 55032 standards.

The result of this measurement ultimately determines whether the signal complies with the standard or not. As seen in the Table 1 above and the chart, the system selected 6 frequencies requiring quasi-peak measurement. In the case of the 100 MHz frequency, the device met the standard, being 0.05 dB below the limit. The high emission at 100 MHz and its harmonics are due to all UST measurement cards connected by a long parallel bus operating at a clock frequency of 100 MHz.

Radiated emissions tests in the frequency range from 1 GHz to 6 GHz, radiated at a distance of 3 meters

Measurements were also performed in a semi-anechoic chamber (SAC). For measurements in the frequency range above 1 GHz, the EUT was placed in the center of the turntable on a non-conductive table 80 cm above the floor, which was partially covered with electromagnetic absorbers to reduce reflections from the floor and simulate conditions as in the FAR (fully anechoic room). The measuring antenna was located 3 meters apart from the EUT and was installed 1m above the floor on the antenna mast, and its polarization (vertical and horizontal) was changing.

Statement of conformity for this test was declared by the disturbance limits defined for class B devices group 1 in PN-EN 55011 [38] and PN-EN 55032 [39] standards and decision rules defined in PN-EN 55016-4-2:2011 [41] standard.

Emission levels were recorded across the 1 GHz to 6 GHz range using a peak detector during preliminary measurements. The test focused on identifying the highest emission levels for each frequency, with all observed values falling significantly below the regulatory thresholds – typically by at least 10 dB. It is important to note that the device is designed to emit intentional signals in the 2.4 GHz Wi-Fi band to support wireless communication. In accordance with the standards, this frequency band was excluded from the conformity assessment. Figure 17 presents the setup used during radiated immunity tests in both the

Table 1. Results from quasi-peak measurements on radiated emissions tests

Frequency (MHz)	QuasiPeak (dBµV/m)	Limit (dBµV/m)	Margin (dB)	Meas. Time (ms)	Bandwidth (kHz)	Height (cm)	Pol	Azimuth (deg)	Corr. (dB)
40.440000	14.21	30.00	15.79	15000.0	120.000	118.0	V	98.0	14.4
46.500000	14.55	30.00	15.45	15000.0	120.000	375.0	V	179.0	10.8
61.020000	4.57	30.00	25.43	15000.0	120.000	393.0	V	-116.0	4.6
99.990000	29.95	30.00	0.05	15000.0	120.000	120.0	V	144.0	9.9
147.960000	17.06	30.00	12.94	15000.0	120.000	137.0	V	-120.0	8.9
624.990000	33.37	37.00	3.63	15000.0	120.000	257.0	H	45.0	20.1

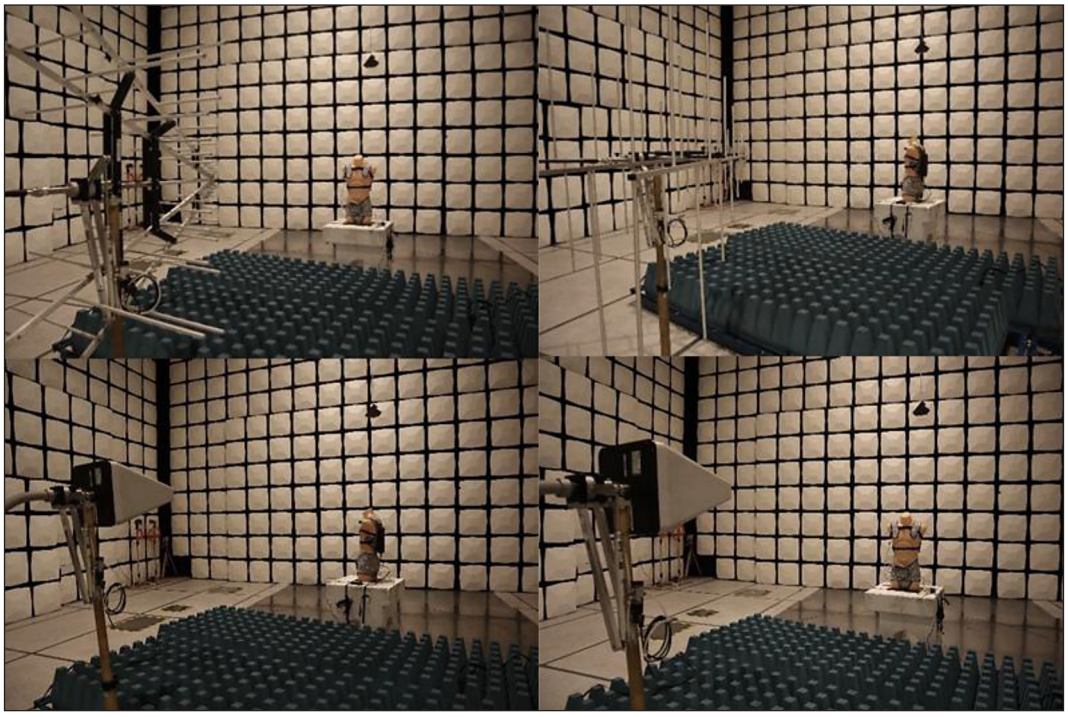

Figure 17. UST/EIT tomograph for monitoring the lower urinary tract mounted on a phantom during radiated immunity test in the frequency range from 80 MHz to 1 GHz and from 1 GHz to 6 GHz

80 MHz to 1 GHz and 1 GHz to 6 GHz ranges, with the tomograph mounted on a phantom under controlled test conditions.

Radiated immunity tests

A radiated, radio-frequency, electromagnetic field immunity test has been carried out according to the procedure defined in PN-EN 61000-4-3 [31] standard, as required in PN-EN 60601-1-2. During radiated immunity tests, the tomograph was exposed to a field with an intensity of 10 V/m at frequencies ranging from 80 MHz to 6 GHz. Four sides of the tested EUT were subjected successively to exposures – horizontal and vertical polarized electric fields.

The EUT was placed within the test volume (plane of calibrated uniform electric field) on a non-conductive support 80 cm above the metallic floor (reference ground plane). During the calibration of this test setup, the part of the floor between the transmitting antenna and the EUT was lined with RF absorbers.

This study assessed whether the electromagnetic field could disrupt or interrupt the device's operation. The investigation during the first tests (design tests) revealed that, with one antenna polarization, issues occurred with the proper functioning of the tomograph. The cause of these problems was identified as the LED strip located on the front of the device, which induced interference and allowed it to propagate to the microcontroller on the main board. This issue was resolved by attaching a ferrite bead to the wire connecting the LED strip and the main board. The final test was successfully completed with a positive result.

Throughout all immunity and emission tests, the tomograph was connected to specially prepared test software monitoring temperature, battery voltage level, charging current level, signals received from ultrasonic and impedance sensors, and the measurement duration. These data served as indicators of the proper operation of the device. The results are shown in Figures 18–19.

ESD immunity tests

Electrostatic discharge immunity tests have been carried out according to the procedure defined in PN-EN 61000-4-2 [29] standard as required in PN-EN 60601-1-2 [26]. During the ESD immunity test, the EUT was placed on a dielectric support above a conducted and grounded plane. Contact discharges were applied when the test generator touched the metallic parts of the EUT, horizontal coupling plane HCP, and vertical coupling plane VCP. Air discharges were applied when the test generator was touched to non-metallic parts.

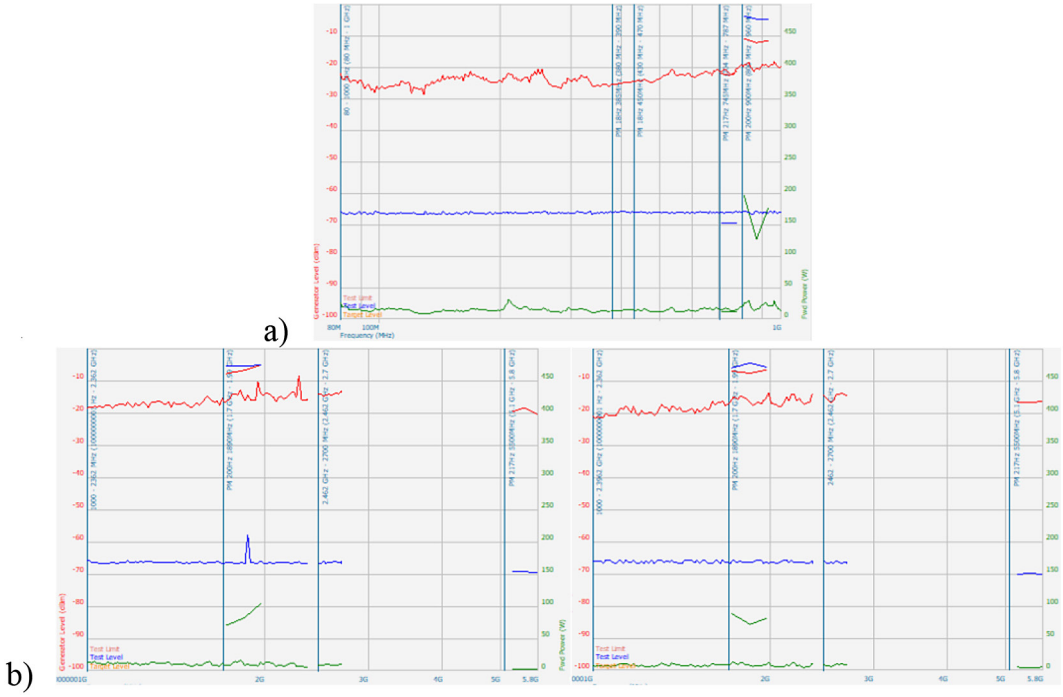

Figure 18. Levels recorded by test setup during radiated, radio-frequency, electromagnetic field immunity test in the SAC a) (80 MHz–1 GHz) for horizontal polarization (blue line – exposure level - E field level, b) (1 GHz–6 GHz) for vertical polarization (left chart) and horizontal polarization (right chart) (blue line – exposure level - E field level

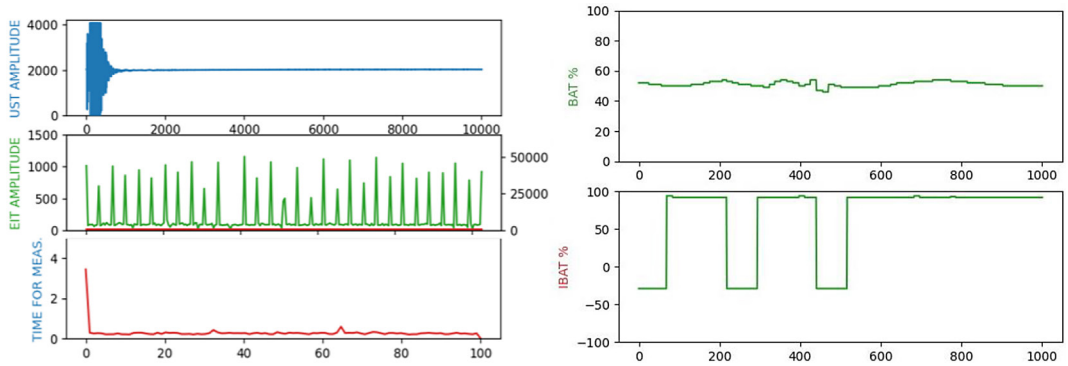

Figure 19. Measured data throughout all immunity and emission tests as indicators of the proper operation of the device

Discharges from the ESD generator were applied to selected points on the EUT's surface, which are accessible to personnel during normal usage. For every one of these points, 10 positive and 10 negative discharges were applied with a minimum 1 s time interval between each one. ESD discharge resistance tests started with a voltage level of 4 kV, which was gradually increased to 8 kV and finally to 15 kV [42]. Air and contact discharges were directed toward the tomograph in a point-and-surface manner. The discharges were also directed toward the EIT electrodes and the UST transducer. The device without USB service cables connected worked continuously during these tests. In the case of connected USB service cables, problems with wired communication occurred already at an 8 kV surge. In the case of these tests, this is an acceptable situation. The device may have trouble communicating with the external system, but should be ready to resume transmission without a power reset. These problems could not be repeated during the final certification tests because all communication is only via Wi-Fi, and the end user cannot access the service USB ports (Figure 20).

Figure 20. UST/EIT tomograph during ESD immunity tests

DISCUSSION

Based on conducted research and prototype work, it has been proven that combining ultrasonic and impedance tomography for long-term bladder monitoring significantly improves diagnostic quality. However, miniaturizing ultrasound tomography for medical applications, especially with UST signals > 2 MHz, is a complex challenge. This complexity arises due to the high speed of UST signals, requiring high-speed measurement analog-to-digital converters (ADCs) (minimum 20 MBPS on each channel). This, in turn, necessitates the use of large and high-speed RAM, the incorporation of FPGA systems, and high-speed communication buses in the measurement system (in the case of this device, a parallel FMC bus). Phased arrays of ultrasound transducers also require symmetrical power supplies of at least +/-50 V with high current efficiency, as the transducer can draw a peak current of several amperes. High voltages and high frequencies on PCBs increase the device's emissions, which, in the case of medical devices, are subject to stricter regulations than those for consumer devices. Additionally, due to the direct contact of impedance measurement electrodes with the patient's body, the device must be galvanically isolated from the power source (charger) for user safety, even when the manufacturer's recommendations prohibit charging during active use. Meeting electromagnetic compatibility requirements also requires the designer to protect all device ports from electrostatic discharges and prevent the leakage of signals that wires as electromagnetic radiation could emit. This is crucial to avoid interference with the operation of other devices. Protecting power ports from emitting signals to the power network is also important. The device must resist the effects of an electromagnetic field over a wide frequency range. It is unacceptable for the influence of the field to interrupt the device's operation, cause restarts, or damage it.

Beyond these engineering challenges, the work presented in this study offers significant scientific value by exploring how two fundamentally different imaging techniques – ultrasound tomography and electrical impedance tomography – can be effectively combined in a wearable format, which aligns with recent developments in wearable EIT systems aimed at real-time monitoring [43]. The hybrid nature of the system allows for the simultaneous acquisition of structural and functional information, which has the potential to improve diagnostic accuracy in cases where conventional imaging provides limited insight. The synchronization of data streams, real-time signal processing, and integration into a miniaturized, power-efficient platform represent an important step forward in the development of multimodal biomedical devices, in line with current trends in wearable ultrasound technology [44].

The proposed solution also addresses an important gap in the current diagnostic tool landscape - the need for non-invasive, portable systems that can operate continuously outside the clinical environment. Its modular design, advanced power management and wireless communication capabilities make it particularly well-suited for pediatric and ambulatory monitoring. These features may support not only improved diagnostics, but also improved patient compliance and comfort, especially for children who require frequent or prolonged assessments. Similar efforts to improve energy efficiency and diagnostic functionality in wearable EIT-based systems have been reported in recent studies focused on bladder monitoring [45]. Although formal clinical trials have not yet been initiated, the device has been

thoroughly tested under laboratory conditions using tissue-mimicking phantoms and specialized testing software. The measurement system and ergonomic sensor interface have been evaluated in scenarios simulating clinical use, with emphasis on hygienic reusability, patient comfort, and signal stability during prolonged use. The integration of EMC-compliant electronics and medically safe interfaces confirms the device's readiness for use in realistic healthcare environments, especially those involving mobile or pediatric care.

Plans are underway to begin preliminary clinical testing to assess diagnostic performance and compare the system's results with conventional imaging modalities. This clinical validation phase is a natural extension of the research and will provide valuable data on diagnostic accuracy, system reliability and usability under real-world conditions. The results of this study are consistent with recent research on hybrid imaging systems and multimodal signal processing. [5, 10] which show promise for improving diagnostic performance by integrating complementary signal sources. However, most previous work has focused on algorithmic simulations or stationary setups and has not addressed the full system-level challenge of combining real-time UST and EIT imaging in a portable format. Issues such as power optimization, EMC compliance, and continuous wireless data transmission remain largely unresolved in the literature [18, 24]. The presented system addresses these gaps by providing a novel framework that integrates hardware miniaturization, real-time multimodal imaging, and medical-grade electromagnetic protection-all within a functional, battery-powered diagnostic platform. Efforts involving sinogram-based reconstruction and deep learning have likewise been explored in the context of stratified flow imaging [46]. Recent studies have explored the challenges associated with multimodal signal integration and hardware optimization in the context of ECT-based imaging applied to industrial two-phase flows [47], further supporting the relevance of hybrid approaches in real-time systems.

Taken together, the proposed solution demonstrates not only technical feasibility and regulatory compliance, but also scientific innovation in the integration of synchronized multimodal imaging into a wearable system. It advances the state of the art in mobile medical diagnostics by solving previously unaddressed engineering and biomedical challenges. This work contributes to ongoing research in intelligent diagnostic devices and may inform future efforts in AI-driven signal interpretation, personalized health monitoring, and next-generation multimodal imaging strategies.

CONCLUSIONS

Using a spectrum analyzer and near-field probe to test your device at every stage of development is the best design practice. Finding the frequencies at which the device emits the most allows the use of low-ESR ceramic capacitors in power supplies, especially converters, and the selection of appropriate ferrite filters for specific current loads. The use of double-sided copper layers to shield wires and long traces on the PCB, the use of trough-hole ferrite beads on long cables, and the use of carefully selected capacitance to smooth sharp signal edges from communications lines or generators. Another option is to shield the PCB's case or other parts that emit strong electromagnetic radiation signals. However, it's important to note that shielding is most effective when it is completely sealed. In many cases, this is a challenge due to the presence of vents. Shielding protects sensitive circuits from surface or point electrostatic discharge (ESD), especially when the enclosure is made of thin material. Another effective way to protect against ESD is to prepare the enclosure with thick material and place the PCBs inside the enclosure as far away from the enclosure walls as possible to provide optimal isolation. This arrangement also improves air circulation inside the device.

This article expounds on the design process of a mobile ultrasound impedance tomograph intended for long-term monitoring of the lower urinary tract. The design process incorporates considerations of miniaturization and electromagnetic compatibility. The integration of ultrasound tomography (UST) and EIT facilitates the acquisition of precise images of the urinary tract while maintaining a compact device configuration. In addition, the process of miniaturization and optimization of energy efficiency contributes to the comfort of use of the device during examinations. A key scientific novelty lies in the successful combination of these two imaging modalities into a single, portable system capable of synchronized data acquisition and real-time operation, which has not been previously implemented in a wearable format.

The developed solution represents a significant advancement in the field of diagnosis of urinary tract diseases. By addressing previously unresolved challenges in hardware integration, signal processing and EMC compliance within a compact platform, the proposed approach opens new perspectives for both technological and clinical innovation. Looking to the future, the innovative approach to the diagnosis of urinary tract disorders opens up new opportunities for the development of this field, introducing modern technologies for the accurate diagnosis and treatment of urinary tract disorders, especially in the pediatric population.

REFERENCES

1. Nieuwhof-Leppink, A.J.; Schroeder, R.P.J.; van de Putte, E.M.; de Jong, T.P.V.M.; Schappin, R. Daytime urinary incontinence in children and adolescents. Lancet Child Adolesc Health 2019, 3.
2. Elale, A.K.; Manilal, A.; Tadesse, D.; Seid, M.; Dubale, A. Magnitude and associated factors of bacterial urinary tract infections among paediatric patients in Arba Minch, Southern Ethiopia. New Microbes New Infect 2023, 51, https://doi.org/10.1016/j.nmni.2023.101083
3. Hay, A.D.; Sterne, J.A.C.; Hood, K.; Little, P.; Delaney, B.; Hollingworth, W.; Wootton, M.; Howe, R.; MacGowan, A.; Lawton, M.; et al. Improving the diagnosis and treatment of urinary tract infection in young children in primary care: Results from the DUTY prospective diagnostic cohort study. Ann Fam Med 2016, 14, 325–336, https://doi.org/10.1370/AFM.1954
4. Lee, H.B.; Lee, S.; Choi, Y.H.; Cheon, J.E.; Lee, S.B.; Cho, Y.J.; Ahn, Y.H.; Lim, S.H. Contrast-enhanced ultrasound for the diagnosis of acute pyelonephritis in pediatric patients with urinary tract infection: A feasibility study. PLoS One 2023, 18, https://doi.org/10.1371/journal.pone.0284016
5. Kłosowski, G.; Rymarczyk, T.; Niderla, K.; Kulisz, M.; Skowron, Ł.; Soleimani, M. Using an LSTM network to monitor industrial reactors using electrical capacitance and impedance tomography – a hybrid approach. Eksploatacja i Niezawodnosc 2023, 25, https://doi.org/10.17531/EIN.2023.1.11
6. Kłosowski, G.; Hoła, A.; Rymarczyk, T.; Mazurek, M.; Niderla, K.; Rzemieniak, M. Use of the double-stage LSTM network in electrical tomography for 3D wall moisture imaging. Measurement 2023, 213, 112741, https://doi.org/10.1016/j.measurement.2023.112741
7. Benba, A.; Akki, M.; Sandabad, S. The application of machine learning on the sensors of smartphones to detect falls in real-time. Informatyka, Automatyka, Pomiary w Gospodarce i Ochronie Srodowiska 2023, 13, https://doi.org/10.35784/iapgos.3459
8. Bilynsky, Y.; Nikolskyy, A.; Revenok, V.; Pogorilyi, V.; Smailova, S.; Voloshina, O.; Kumargazhanova, S. Convolutional neural networks for early computer diagnosis of child dysplasia. Informatyka, Automatyka, Pomiary w Gospodarce i Ochronie Srodowiska 2023, 13, https://doi.org/10.35784/iapgos.3499
9. Pawlik, P.; Kania, K.; Przysucha, B. Fault diagnosis of machines operating in variable conditions using artificial neural network not requiring training data from a faulty machine. Eksploatacja i Niezawodnosc 2023, 25, https://doi.org/10.17531/ein/168109
10. Maciura, Ł.; Wójcik, D.; Rymarczyk, T.; Król, K. Novel hybrid algorithm using convolutional autoencoder with SVM for electrical impedance tomography and ultrasound computed tomography. Informatyka, Automatyka, Pomiary w Gospodarce i Ochronie Środowiska 2023, 13, 4–9, https://doi.org/10.35 https://doi.org/784/IAPGOS.3377
11. Rząsa, M. Assessment of benefits resulting from the use of computer control systems in precision agriculture. Bulletin of the Polish Academy of Sciences Technical Sciences 2023, 144582–144582, https://doi.org/10.24425/BPASTS.2023.144582
12. Kumar, A.; Byakodi, K.G.; Chandrapattan, P.P.; Teggimani, V. Efficacy and comparison of appendicitis inflammatory response score with alvarado score in predicting the diagnosis of acute appendicitis. International Surgery Journal 2019, 6, https://doi.org/10.18203/2349-2902.isj20193328
13. Ohira, S.; Komiyama, R.; Kanayama, N.; Sakai, K.; Hirata, T.; Yoshikata, K.; Ueda, Y.; Miyazaki, M.; Nakayama, M.; Koizumi, M.; et al. Improvement in bladder volume reproducibility using a-mode portable ultrasound bladder scanner in moderate-hypofractionated volumetric modulated arc therapy for prostate cancer patients. J Appl Clin Med Phys 2022, 23, https://doi.org/10.1002/acm2.13546
14. Li, R.; Gao, J.; Li, Y.; Wu, J.; Zhao, Z.; Liu, Y. Preliminary study of assessing bladder urinary volume using electrical impedance tomography. J Med Biol Eng 2016, 36, d https://doi.org/10.1007/s40846-016-0108-1
15. MAX2082 datasheet Low-Power, High-Performance Octal Ultrasound Transceiver with Integrated AFE, Pulser, T/R Switch, and CWD Beamformer.
16. Ali, R.; Brevett, T.; Zhuang, L.; Bendjador, H.; Podkowa, A.S.; Hsieh, S.S.; Simson, W.; Sanabria, S.J.; Herickhoff, C.D.; Dahl, J.J. Aberration correction in diagnostic ultrasound: A review of the prior field and current directions. Z Med Phys 2023, 33.
17. Zhang, Y.; Demosthenous, A. Integrated circuits

for medical ultrasound applications: imaging and beyond. IEEE Trans Biomed Circuits Syst 2021, 15, doi:10.1109/TBCAS.2021.3120886.

18. Kidav, J.; Pillai, P.M.; Deepak, V.; Sreejeesh S., G. Design of a 128-Channel transceiver hardware for medical ultrasound imaging systems. IET Circuits, Devices & Systems 2022, 16, 92–104, https://doi.org/10.1049/CDS2.12087
19. Krambeck, L.; Baptista Nishida, F.; Marrone De Aguiar, V.; Dias Dos Santos, P.H.; Antonini Alves, T. Thermal performance evaluation of different passive devices for electronics cooling. Thermal Science 2019, 23, https://doi.org/10.2298/TSCI170610300K
20. Maroti, P.K.; Padmanaban, S.; Holm-Nielsen, J.B.; Sagar Bhaskar, M.; Meraj, M.; Iqbal, A. A new structure of high voltage gain SEPIC converter for renewable energy applications. IEEE Access 2019, 7, https://doi.org/10.1109/ACCESS.2019.2925564
21. Agarwal, M.; Tomar, A.; Kumar, N. An IEEE single-precision arithmetic based beamformer architecture for phased array ultrasound imaging system. Engineering Science and Technology, an International Journal 2021, 24, https://doi.org/10.1016/j.jestch.2021.03.005
22. Hu, C.L.; Li, C.J.; Cheng, I.C.; Sun, P.Z.; Hsu, B.; Cheng, H.H.; Lin, Z.S.; Lin, C.W.; Li, M.L. Acoustic-field beamforming-based generalized coherence factor for handheld ultrasound. Applied Sciences (Switzerland) 2022, 12, https://doi.org/10.3390/app12020560
23. Zhang, X.; Xu, Y.; Wang, N.; Jiao, Y.; Cui, Y. A novel approach to tele-ultrasound imaging: compressive beamforming in fourier domain for ultrafast ultrasound imaging. Applied Sciences (Switzerland) 2023, 13, https://doi.org/10.3390/app13053127
24. Kang, J.; Kim, P.; Yoon, C.; Yoo, Y.; Song, T.K. Efficient parallel-beamforming based on shared FIFO for ultra-compact ultrasound imaging systems. IEEE Access 2020, 8, 80490–80501, https://doi.org/10.1109/ACCESS.2020.2990790
25. Lin, X.; Shi, H.; Fu, Z.; Lin, H.; Chen, S.; Chen, X.; Chen, M. Dynamic speed of sound adaptive transmission–reflection ultrasound computed tomography. Sensors 2023, 23, https://doi.org/10.3390/s23073701
26. PN-EN 60601-1-2:2015-11 (EN 60601-1-2:2015) Standard Medical Electrical Equipment - Part 1-2: General Requirements for Basic Safety and Essential Performance - Collateral Standard: Electromagnetic Disturbances - Requirements and Tests.
27. PN-EN 61000-4-4:2013-05 (EN 61000-4-4:2012) Standard Electromagnetic Compatibility (EMC) - Part 4-4: Testing and Measurement Techniques - Electrical Fast Transient/Burst Immunity Test.
28. PN-EN 61000-4-5:2014-10 + A1:2018-01 (EN 61000-4-5:2014 + A1:2017) Standard Electromagnetic Compatibility (EMC) - Part 4-5: Testing and Measurement Techniques - Surge Immunity Test.
29. PN-EN 61000-4-2:2011 (EN 61000-4-2:2009) Standard Electromagnetic Compatibility (EMC) - Part 4-2: Testing and Measurement Techniques - Electrostatic Discharge Immunity Test.
30. PN-EN 61000-4-6:2014-04 (EN 61000-4-6:2014) Standard Electromagnetic Compatibility (EMC) - Part 4-6: Testing and Measurement Techniques - Immunity to Conducted Disturbances, Induced by Radio-Frequency Fields.
31. PN-EN 61000-4-3:2021-06 (EN IEC 61000-4-3:2020) Standard Electromagnetic Compatibility (EMC) - Part 4-3 : Testing and Measurement Techniques - Radiated, Radio-Frequency, Electromagnetic Field Immunity Test.
32. PN-EN 61000-4-8:2010 (EN 61000-4-8:2010) Standard Electromagnetic Compatibility (EMC) - Part 4-8: Testing and Measurement Techniques - Power Frequency Magnetic Field Immunity Test.
33. PN-EN 61000-4-11:2020-11 (EN IEC 61000-4-11:2020) Standard Electromagnetic Compatibility (EMC) - Part 4-11: Testing and Measurement Techniques - Voltage Dips, Short Interruptions and Voltage Variations Immunity Tests for Equipment with Input Current up to 16 A per Phase.
34. 34. PN-EN 55016-2-1:2014-09 + A1:2017-12 (EN 55016-2-1:2014 + A1:2017) Standard Specification for Radio Disturbance and Immunity Measuring Apparatus and Methods - Part 2-1: Methods of Measurement of Disturbances and Immunity - Conducted Disturbance Measurements.
35. PN-EN 55016-2-3:2017-06 + A1:2020-01 (EN 55016-2-3:2017 + A1:2019) Standard Specification for Radio Disturbance and Immunity Measuring Apparatus and Methods - Part 2-3: Methods of Measurement of Disturbances and Immunity - Radiated Disturbance Measurements.
36. PN-EN 61000-3-2:2019-04 + A1:2021-08 (EN IEC 61000-3-2:2019 + A1:2020) Standard Electromagnetic Compatibility (EMC) - Part 3-2: Limits - Limits for Harmonic Current Emissions (Equipment Input Current ≤16 A per Phase.
37. PN-EN 61000-3-3:2013-10 + A1:2019-10 + A2:2022-04 (EN 61000-3-3:2013 + A1:2019 + A2:2021) Standard Electromagnetic Compatibility (EMC) - Part 3-3: Limits - Limitation of Voltage Changes, Voltage Fluctuations and Flicker in Public Low-Voltage Supply Systems, for Equipment with Rated Current ≤16 A per Phase and Not Subject to Conditional Connection.
38. PN-EN 55011:2016-05 + A1:2017-06 + A2:2021-08 (EN 55011:2016 + A1:2017 + A2:2021) Industrial, Scientific and Medical Equipment - Radio-Frequency Disturbance Characteristics - Limits and

Methods of Measurement.

39. PN-EN 55032:2015-09 + A1:2021-05 (EN 55032:2015 + A1:2020) Electromagnetic Compatibility of Multimedia Equipment - Emission Requirements.
40. Krawczyk, A.; Korzeniewska, E. Some Aspects of Electromagnetic Field Shielding. Przeglad Elektrotechniczny 2023, 99, doi:10.15199/48.2023.03.22.
41. PL-EN 55016-4-2:2011 (EN 55016-4-2:2011) Specification for Radio Disturbance and Immunity Measuring Apparatus and Methods - Part 4-2: Uncertainties, Statistics and Limit Modelling - Measurement Instrumentation Uncertainty.
42. Ker, M.D.; Yen, C.C.; Shih, P.C. On-chip transient detection circuit for system-level ESD protection in CMOS integrated circuits to meet electromagnetic compatibility regulation. IEEE Trans Electromagn Compat 2008, 50, https://doi.org/10.1109/TEMC.2007.911911
43. Pennati, F.; Angelucci, A.; Morelli, L.; Bardini, S.; Barzanti, E.; Cavallini, F.; Conelli, A.; Di Federico, G.; Paganelli, C.; Aliverti, A. Electrical impedance tomography: from the traditional design to the novel frontier of wearables. Sensors 2023, 23, 1182, https://doi.org/10.3390/S23031182
44. Huang, H.; Wu, R.S.; Lin, M.; Xu, S. Emerging wearable ultrasound technology. IEEE Trans Ultrason Ferroelectr Freq Control 2024, 71, 713–729, https://doi.org/10.1109/TUFFC.2023.3327143
45. Mazurek, M.; Dziadosz, M.; Rymarczyk, T.; Wójcik, D.; Gryniewicz-Jaworska, M.; Słoniec, J. Assessing energy efficiency and the application of artificial neural networks in wearable sensors using electrical impedance tomography. Advances in Science and Technology. Research Journal 2025, 19.
46. Mayet, A.M.; Shahsavari, M.H.; Alizadeh, S.M.; Hanus, R.; Parayangat, M.; Raja, R.M.; Muqeet, M.A.; Salman, M.A.; Kubiszyn, P. A Novel approach for measuring the void fraction in stratified air-water systems utilizing an 8-Blade capacitance-based sensor, sinogram, and a deep neural network. Advances in Science and Technology. Research Journal 2025, 19, 269–283, https://doi.org/10.12913/22998624/195454
47. Wajman, R.; Nowakowski, J.; Łukiański, M.; Banasiak, R. Machine learning for two-phase gas-liquid flow regime evaluation based on raw 3D ECT measurement data. Bulletin of the Polish Academy of Sciences: Technical Sciences 2024, 72, https://doi.org/10.24425/BPASTS.2024.148842